Tectonophysics 812 (2021) 228912

Contents lists available at ScienceDirect

Tectonophysics

journal homepage: www.elsevier.com/locate/tecto

Cenozoic structure and tectonics of North subbasins in Beibu Gulf Basin, northern South China Sea

Yiming Liu [a,b,c,*], Zhiping Wu [a,c,*], Lijun Liu [b,**], Shiyong Yan [a,c], Lin Hu [d], Mingming Ping [a], Meng Zhang [a]

[a] Department of Geology, China University of Petroleum (East China), Qingdao 266580, China
[b] Department of Geology, University of Illinois at Urbana-Champaign, Urbana, IL 61820, USA
[c] Shandong Provincial Key Laboratory of Deep Oil and Gas, Qingdao 266580, China
[d] Exploration and Development Institute, Zhanjiang Branch of CNOOC, Zhanjiang 524057, China

ARTICLE INFO

Keywords:
Rifting
NE-striking faults
Strike-slip reactivation
Tectonic transition
Beibu Gulf basin
Northern South China Sea

ABSTRACT

The spatial and temporal interaction of rifting at the northern South China Sea (SCS) margin and shearing along Red River Fault Zone (RRFZ) is crucial to understanding the regional geodynamics. Their obscure relationship has led to controversial models for the origin of the Beibu Gulf basin within the northeast edge of the SCS. Newly released seismic-reflection data and well logs permit a new comprehensive analysis of the tectono-sedimentary history, which provides important constraints on the basin-forming history. Based on the interpretation of 3D multi-channel seismic data, we analyzed the seismic stratigraphy, fault development and tectonic subsidence, with additional confirmation from analogue modelling. The results suggest that several key unconformities separate the rifting history of North subbasins into three distinct phases. The *syn*-depositional faults and depocenters experienced a tectonic transition from NE- to NNE-orientated during the first two stages. The extensional structures were overprinted by the conjugate strike-slip faulting during stage III (30–23 Ma), as evidenced by the NEE-trending predominant faults and reactivation of NW-trending blind faults. Together with other regional geologic records and plate reconstruction history, we propose an updated view of the region's tectonic history. The NE-trending rift system initiated at the beginning of the Cenozoic. Tectonic reconfiguration at ~40 Ma induced a regional change of stress field to become north-south stretching that caused a tectonic transition of the basin. Influenced by the regional shearing activity of the RRFZ as well as additional north-south stretching, the basin was reworked by widespread strike-slip deformation. We therefore emphasize that while the basin's overall architecture was defined by the development of NE-trending rifts, both reconfiguration of the stress field acting on pre-existing faults and strike-slip reactivation of blind faults led to the basin's current intricate structure.

1. Introduction

The northern margin of the South China Sea (SCS) preserves important information for the region's tectonic evolution from continental rifting to seafloor spreading (e.g. Cullen et al., 2010; Franke et al., 2014; Ding et al., 2018). However, the relationship between the continental margin rifting and shearing due to the Red River Fault Zone (RRFZ) is still ambiguous. The North subbasins of Beibu Gulf basin (BGB) are located at the intersection of these two dynamic systems, making it an ideal site for investigating extensional and shearing tectonics. Although these tectonic activities have profound influence on the evolution of continental margins, little is known about the detailed basin history due to the lack of high-resolution seismic reflection data and meticulous strata chronology. The obscure relationship between crustal deformation and surface sedimentary processes results in variable and controversial interpretations of offshore basin evolution (e.g. Hu et al., 2013; Zhang et al., 2013;Franke et al., 2014; Zhao et al., 2018; Liu et al., 2021b).

Influenced by the complex interactions between the west-Pacific convergent boundary and multiple microplates formed during the closure of the Tethys (Morley, 2002; Yin, 2010; Li et al., 2019), evolution of the BGB reflects the superposition of various stress fields and

* Corresponding authors at: Department of Geology, China University of Petroleum (East China), Qingdao 266580, China.
** Corresponding authors at: Department of Geology, University of Illinois at Urbana-Champaign, Urbana, IL 61801, USA.
E-mail addresses: lymupc@126.com (Y. Liu), wuzp@upc.edu.cn (Z. Wu), ljliu@illinois.edu (L. Liu).

https://doi.org/10.1016/j.tecto.2021.228912
Received 6 January 2020; Received in revised form 22 April 2021; Accepted 4 May 2021
Available online 12 May 2021

tectonic structures. Consequently, its tectono-sedimentary history displays considerable spatial and temporal variations. Although numerous studies have been carried out concerning the fault tectonics and its control on sedimentation in the BGB (e.g., Li et al., 2012; Tong, 2012; Ma et al., 2014), the origin of the basin remains unclear. In particular, the role of strike-slip deformation in basin evolution is debatable. Previous studies consider the BGB to be a pull-apart basin associated with a set of right-stepping, NE-trending dextral strike-slip faults (Wei et al., 2008; Ma et al., 2014). In these models, the strike-slip system dies out to the northeast in a horse-tail-like splay, whose formation resulted in the North subbasins of the BGB. However, the characteristics of boundary faults reveal sustained extension during the *syn*-rift stage, and do not accommodate strike-slip displacement. Some scholars suggest instead that BGB is a rift basin developed on the passive margin due to reorientation of the regional stress field (Li et al., 2012; Tong, 2012). In short, the current interpretations of BGB evolution have reached little consensus, and further clarification of the spatial and temporal interaction between extensional and shearing deformation is necessary.

Given that the BGB plays a crucial role in understanding the dynamic interaction between the Pacific realm and the Tethyan realm (Franke et al., 2014), a detailed basin analysis followed by a re-evaluation of the tectonic evolution is overdue. In this study, we seek to address the spatial and temporal variations of intricate basin structures by presenting and interpreting the newly released high-quality 3D seismic-reflection images and borehole data. Combining this analysis with regional-scale geologic records and plate reconstruction, we propose an updated view on the basin's tectonic history. This study provides new evidence on the tectonic evolution of the northern SCS margin, and sheds new light on future studies of the tectonic evolution of Southeast Asia.

2. Geological setting

2.1. Regional setting

The continental margin along northern SCS is tectonically situated at the junction of the Eurasian, Pacific, and Indo-Australian Plates and it experienced widespread deformation since the Mesozoic (Li and Li, 2007; Ye et al., 2018; Zhang and Li, 2018). During the Paleogene, the paleo-stress field changed from compression to extension as a result of roll-back or steepening of the Pacific slab (Taylor and Hayes, 1983; Ding et al., 2020; Liu et al., 2021a). The continuous subduction induced episodic rifting on the continental margin. Two main rift events can be distinguished in the Cenozoic and the latter event resulted in the formation of the South China Sea (Franke et al., 2014). Published data reveal that the seafloor spreading of the SCS initiated at ~32 Ma (Briais et al., 1993; Savva et al., 2014; Li et al., 2015), and the spreading ceased at about 15 Ma (Li et al., 2015). Most authors agree that seafloor spreading initiated in the East Sub-basin, followed by a ridge jump and reorientation to the Southwest Sub-basin (Briais et al., 1993; Ding et al., 2018; Sun et al., 2019). The diachronous opening of the ocean basin from east to west progressively triggered the tectonic transitions of different basins.

The large-scale displacement RRFZ is a first-order tectonic feature in the region (Fig. 1a), along which the Indochina Block moved during the collision between Indian and Eurasian Plates (Tapponnier et al., 1990; Leloup et al., 2001). However, both the sense and timing of this displacement remain heavily debated (Clift and Sun, 2006; Zhao et al., 2018; Rangin et al., 1995; Leloup et al., 2001). Some studies suggested that the sinistral motion of the RRFZ occurred between 35 and 17 Ma (Leloup et al., 2001; Gilley et al., 2003; Zhu et al., 2009). Searle (2006) proposed instead that the sinistral motion should be limited to 32–22 Ma. Geochronology analyses further constrained the sinistral deformation to be 28–21 Ma (Cao et al., 2011; Liu et al., 2015). Conversely, a few tens of kilometers of right lateral motion was proposed to have occurred along the southern part of the RRFZ during the opening of the SCS (Sibuet et al., 2016). Given the apparently significant influence of RRFZ on the evolution of the offshore basins (Lei et al., 2015; Zhao et al., 2018), analyzing the basins' structural features could help better constrain the tectonic history of the RRFZ.

2.2. Basin overview

The BGB is located at the intersection of the northern SCS margin and the lithospheric-scale strike-slip RRFZ (Fig. 1a). It is a significant Cenozoic petroliferous basin with a rhombic shape and a total area of 3.98×10^4 km^2 (Gao et al., 2019). The basement of the basin consists mostly of Upper Paleozoic metamorphic rocks. Locally, Late Cretaceous

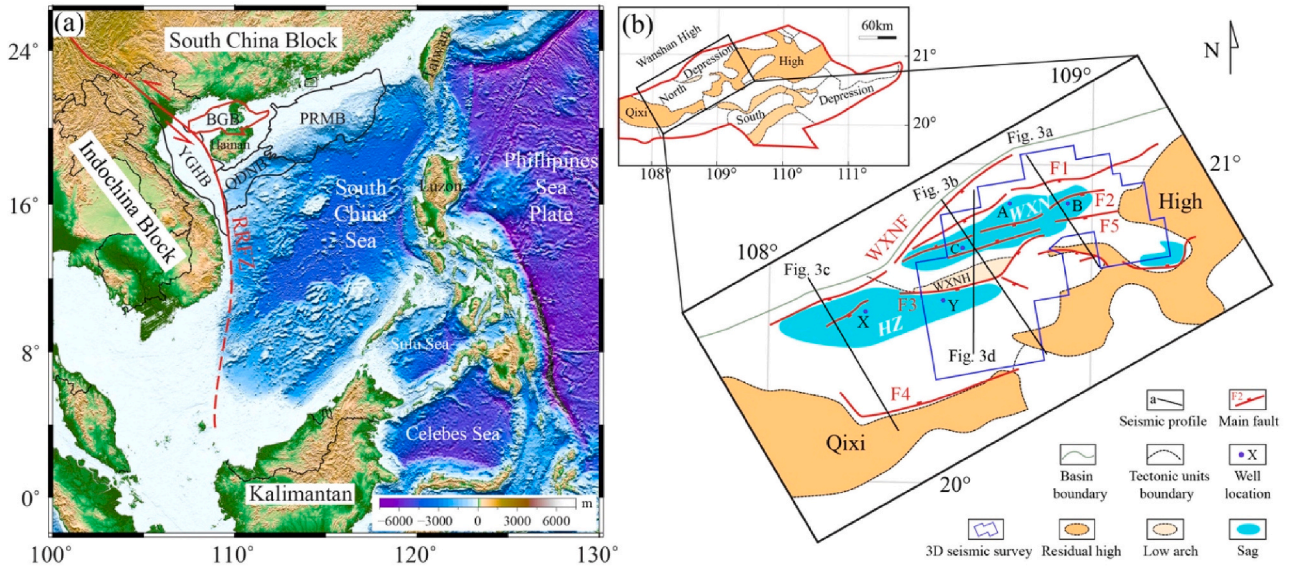

Fig. 1. Regional location and tectonic units of Beibu Gulf basin. Abbreviations: BGB: Beibu Gulf basin, PRMB: Pearl River Mouth Basin, YGHB: Yinggehai Basin, QDNB: Qiongdongnan Basin, RRFZ: Red River Fault Zone, WXNH: Weixinan high, WXN: Weixinan subbasin, HZ: Haizhong subbasin, WXNF: Weixinan fault. F1: No.1 fault. F2: No.2 fault, etc. The purple dots show the well locations used in Fig. 5 and the capitalized A, B, C, X, Y indicate names of the wells. The a, b, c, d indicate the locations of cross-sections in Fig. 3. (For interpretation of the references to colour in this figure legend, the reader is referred to the web version of this article.)

redbeds underlie the oldest strata of the basin (Sun et al., 2014). The Qixi high separates the basin into two sub-basins, namely the North subbasins and the South subbasin (Fig. 1b). The BGB archives a long-term terrestrial and marine sedimentary record during two distinct Cenozoic stages (Huang et al., 2013; Chen et al., 2019). During the first stage, the Paleogene *syn*-rift stage, accommodation space for deposition developed when normal faulting produced grabens and half grabens. During the second stage, the Neogene post-rift stage, the basin manifested as a depression following isostatic adjustment due to thermal re-equilibration (Franke et al., 2014). Neogene strata covered grabens and half grabens as well as surrounding areas. A regional angular unconformity separates of the syn-rift strata from the post-rift ones, indicating that widespread erosion took place prior to the Neogene deposition. This two-stage evolution is consistent with that of most rift basins around marginal seas offshore China, such as the Bohai Bay basin in North China, East China Sea basin, and the Pearl River Mouth basin in the northern edge of the SCS (Ren et al., 2002).

The North subbasins, our main study area, are confined on the northwest by the Wanshan high and on the southeast by the Qixi high (Fig. 1b). It mainly consists of Weixinan subbasin and Haizhong subbasin, separated by the F3 fault along the Weixinan high. The North subbasins are bounded by three major faults, the Weixinan fault, dipping towards the southeast, the F1 fault, dipping towards the south-southeast, and the F4 fault, dipping towards the northwest. The basin has experienced several distinct deformation events, likely in response to the RRFZ, the west-Pacific subduction, as well as the Indo-Australian subduction (Hall and Spakman, 2015; Ren, 2018In succession, from oldest to youngest, these events are named: the Shenhu event, the Zhuqiong event, the Nanhai event, and the Dongsha event (Ren et al., 2002). Each event either produced a new set of faults or resulted in reactivation of existing faults. Therefore, movement of the primary fault system in the basin (i.e., the NE-, ENE-, EW- and NW-trending faults) resulted in prominent temporal and spatial variations.

3. Data and methods

This study utilizes new marine seismic-reflection data, together with logs from drill holes, collected during 2010 to 2017 in the North subbasins of the BGB. The seismic database, obtained using geophysical survey vessels of the China National Offshore Oil Company (CNOOC), includes 2-D profiles of ship tracks with a total length of 3500 km, and 3-D blocks covering an area of 5000 km^2. Multi-channel seismic lines were acquired by 576 channels with a shot-point spacing of 37.5 m and a common midpoint spacing of 12.5 m. The seismic volume was processed to a main frequency bandwidth of 30–45 Hz, with a common mid-point spacing of 12.5 m, and a recording length of 7 s TWT. The data was processed using GeoEast and CGG software (Xu et al., 2016; Tian et al., 2019) in the facilities of Seismic Data Processing Center in CNOOC. Most of the 2-D seismic profiles cover the Haizhong subbasin. About 70% of these trend NW-SE, perpendicular to the subbasin's axis, while the remainder trend NE-SW, parallel to the basin's axis. The 3-D seismic blocks cover the main body of the basin. Drilling and logging data from more than 100 drillholes were used to aid in stratigraphic correlation. All these data belong to the Zhanjiang Oil Branch of CNOOC.

To integrate the seismic reflection data with the logging data, the Exploration and Development Institute of CNOOC produced a synthetic seismic profile based on well data, with which we calibrated our data, especially to verify the accuracy of our seismic horizon interpretation in the Cenozoic section. On the basis of our seismic interpretation, we produced maps for the spatial distribution of faults, and constructed the basin's depth structure. The above interpretation was conducted using the *GeoFrame system* provided by Schlumberger Limited company (Sheaf et al., 2003; Zampetti et al., 2004). With our seismic constraints on stratigraphy, together with constraints on compaction corrections obtained from 20 well logs, we were able to develop a model of the subsidence history in several wells using *BasinView software* provided by Platte River Associates, Inc. (Zuo et al., 2011). To evaluate the subsidence history of the North subbasins, we applied the commonly adopted one-dimensional local isostatic backstripping analysis (Van Hinte, 1978; Allen and Allen, 2013) to five different sub-sags of the basin that have continuous stratigraphic records. We then calculated the total subsidence and tectonic subsidence through time after correcting sediment decompaction for each lithology and paleobathymetry (Duan et al., 2020). With our subsidence history models, we utilized *Petrel software* to produce maps of stratal thickness at various stages of basin evolution. At last, in order to understand how temporal changes in the stress field could have influenced the fault activity in the basin, we carried out a series of sandbox analogue modelling experiments in a 35 cm-long by 30 cm-wide box. In these experiments, we used a 5 cm-thick layer of dry quartz sand (effectively a Coulomb material) with a grain size between 74 and 96 μm to represent sedimentary strata. Rigid cystosepiment blocks were used to represent residual highs and pre-existing faults in the basin. A canvas and rubber layer under the sands represented the top surface of basement. We adopted a scaling factor of 10^5 for length, as widely used for sandbox experiments designed to represent the behavior the Earth's brittle upper crust (McClay and White, 1995; Hampel et al., 2004; Panien et al., 2006; Marshak et al., 2019). In addition, the velocity of the driving unit is fixed at 0.1 mm/s and we take photo records with a 10-s interval.

4. Results

4.1. Seismic stratigraphy in the North subbasins

The stratigraphic framework of the BGB (Fig. 2) was established by the correlating horizons in seismic-reflection profiles and stratigraphic features in blocks and drilling logs. It is worth noting that several angular unconformities separate the stratigraphic section of the basin into different formations. Horizon Tg is a prominent unconformity that separates the Mesozoic basement from overlying basin strata, and therefore represents the onset of rifting. Early rift fluvial sediments of the Changliu Formation (Huang et al., 2013), deposited between Paleocene and Early Eocene, overlie the Tg unconformity. Borehole data reveal that this formation consists of yellowish sandstone and glutenite. It appears as a discontinuous, low-amplitude seismic reflector (Fig. 2a). The overlying Liushagang Formation (ca. 55.8–33.9 Ma) represents the *syn*-rift phase of lacustrine deposition and mainly consists of bluish-grey mudstone and shale with interbeds of sandstone. Different members of the Liushagang Formation (including El^3, El^2, El^1 member) differ from one another on seismic-reflection profiles. Specifically: the El^3 formation appears as a continuous, high-amplitude reflector (Fig. 2a), the El^2 formation appears as a continuous, parallel, low-amplitude reflector (Fig. 2a), and the El^1 appears as a continuous moderate-amplitude reflector (Fig. 2a). The Weizhou Formation (subdivided into three members, known as Ew^3, Ew^2, Ew^1) consists of bluish-grey sandstone that is interbedded with mudstone and shale (Fig. 2b). On seismic-reflection profiles, it appears as a continuous, high-amplitude reflector (Fig. 2a). Horizons T3 and T5 separate the rifting evolution of the basin into three distinct rift stages, i.e. the initial *syn*-rift stage I (65.5–40.4 Ma), the reworked syn-rift stage II (40.4–30.3 Ma), and the transtensional syn-rift stage III (30.3–23 Ma).

The T1 unconformity is characterized by a clear truncation relation with the strata underneath (Fig. 2a). It represents the erosion surface that was developed synchronously with initial lithosphere break-up, and separates the *syn*-rift strata below from the post-rift strata above. Faults are either truncated at the unconformity without offsetting strata above the unconformity, or display a marked decrease in displacement across the unconformity with less displacement above. This feature indicates that the faults were active before the unconformity and then were reactivated subsequently. Overlying Horizon T1 is the post-rift interval when the basin started to suffer marine transgression. The transitional facies strata above the unconformity tend to be continuous, low-

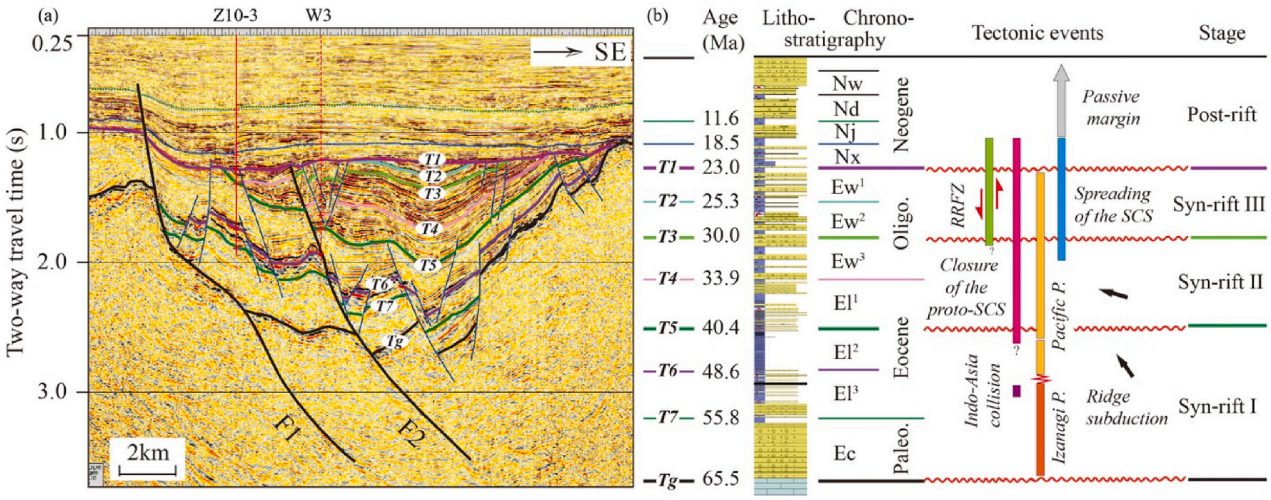

Fig. 2. The seismic stratigraphic framework of the North subbasins in BGB. Lines with different colors in (a) indicate the stratigraphic boundaries. The colorful bars in (b) indicate the duration of different tectonic events.

amplitude reflectors (Fig. 2a). Drilling data indicate that the syn-rift strata were deposited predominantly in lacustrine environments, and a distinct change of the depositional environments can be identified during the post-rift stage (Huang et al., 2014).

4.2. Seismic data interpretation

The profiles traversing the North subbasins (Fig. 3) indicate that the NE-NEE trending faults determine the structural framework of the basin. The wedge-shaped *syn*-rift strata are overlain by the relative flat post-rift strata, and it is characterized by faulted blocks and half-grabens (Figs. 3a, b). As the border fault of the Weixinan subbasin, the NE-trending F1 fault presents as a listric or stairstep fault with a long offset, implying a long-lived extensional deformation history. The transtensional F2 fault in the central subbasin is characterized by a negative flower structure in cross section, which is demonstrated by a series of small-scale faults attached on the listric main fault, making the internal structure of the half-graben more complex. Whereas the flexurally deformed strata within the flower structure represent the overprint of shortening deformation (Fig. 3b).

The evolving Weixinan fault and F3 fault control the sustained extension of the Haizhong subbasin. Influenced by the listric geometry of the border faults, the subbasin presents an asymmetric half-graben morphology, accompanied by the southeastward thinning of the *syn*-rift strata. The sustained normal faulting of border faults controls the wedge-shaped syn-rift strata, the uppermost of the which were strongly denudated in the Late Paleogene, along the striking T1 angular unconformity. The strata below the uniformity are offset by the normal faults that extend into the basement, while the strata above are barely influenced by the faults. The remarkable folding and reverse faulting in Fig. 3c reveal that the basin experienced a tectonic inversion during the Late Neogene.

In terms of the minor faults, two distinct groups of fault system could be identified. The first group was confined between Horizon T5 and Tg. Numerous newborn minor faults emerged closely together and cut cross the T6 and T7 unconformities (Figs. 3a, b). Its occurrence is simultaneous with the large offsetting of border faults, implying intensive rifting during stage I. Another group of minor faults tend to cut through the Horizon T1 or T2 (Figs. 3a, d). It is characterized by a flower structure of which minor fault cluster attaches on a long-term main fault, indicating the overprint of shearing deformation.

4.3. Syn-depositional fault system in different stages

The detailed mapping of the syn-rift fault system allows a systematic investigation of fault evolution. The extensional fault system within the study area has an overall NE-ENE strike, which is consistent with the predominant trend of faulting in the northern margin of South China Sea (e.g. Zhang et al., 2013; Zhao et al., 2020). Several major faults dominate the basin evolution during the rifting process, especially the NE-ENE directed Weixinan faults, F1 fault and F3 fault, each of which is a long-term active basin-controlling or subbasin-controlling fault (Fig. 3). These faults preferred a curved morphology in map view and can be roughly divided into several segments based on along-strike variations (Fig. 4a). The variable distribution of *syn*-depositional faults allows us to recognize three fault systems related to distinct tectonic events. Two phases of extension and one phase of transtension were identified. The NE- and ENE-trending extensional systems are widely distributed within the entire subbasin. While the conjugate NW and ENE strike-slip faults system are regularly distributed along pre-existing fault zones.

4.3.1. The NE-striking extensional fault system

Faults belonging to the NE-striking fault system tend to dip southeast. The major faults typically show a large fault heave (Figs. 4a, b), which indicates the dominant NW-SE oriented stretching during the stage I. The initial normal faulting of NE-trending Weixinan fault and F1 fault determines the embryonic form of the two independent subbasins, respectively (Figs. 4a). Meanwhile, a large number of small-scale ENE-striking faults developed with an average azimuth of 76.8° during the deposition of El^2 sub-sequence (48.6–40.4 Ma) (Fig. 4b), consistent with the cross-section characteristics across the northern part of the basin (Figs. 3b, d). The large dip-slip faulting rates (exceed 75 m/Ma) of major faults (Figs. 4f) and the occurrence of many minor faults within the confined Weixinan subbasin mark the intensive extension during the rifting process.

4.3.2. The ENE/EW-striking extensional fault system

The ENE extensional fault system dominated the basin evolution during stage II, suggesting the clockwise rotation of the stress field. Although an overall decrease of the heave amount could be detected from the Figs. 4c, d, the ENE-EW-striking F3 fault manifested a larger heave amount in comparison to the NE-striking faults. Dip-slip faulting rates of the NE-trending Weixinan fault decreased sharply to less than 20 m/Ma, while the ENE/EW-trending faults with a dip-slip faulting rate above 75 m/Ma dominated the basin evolution during stage II. The evolution of *syn*-depositional fault indicates the stress field changed to

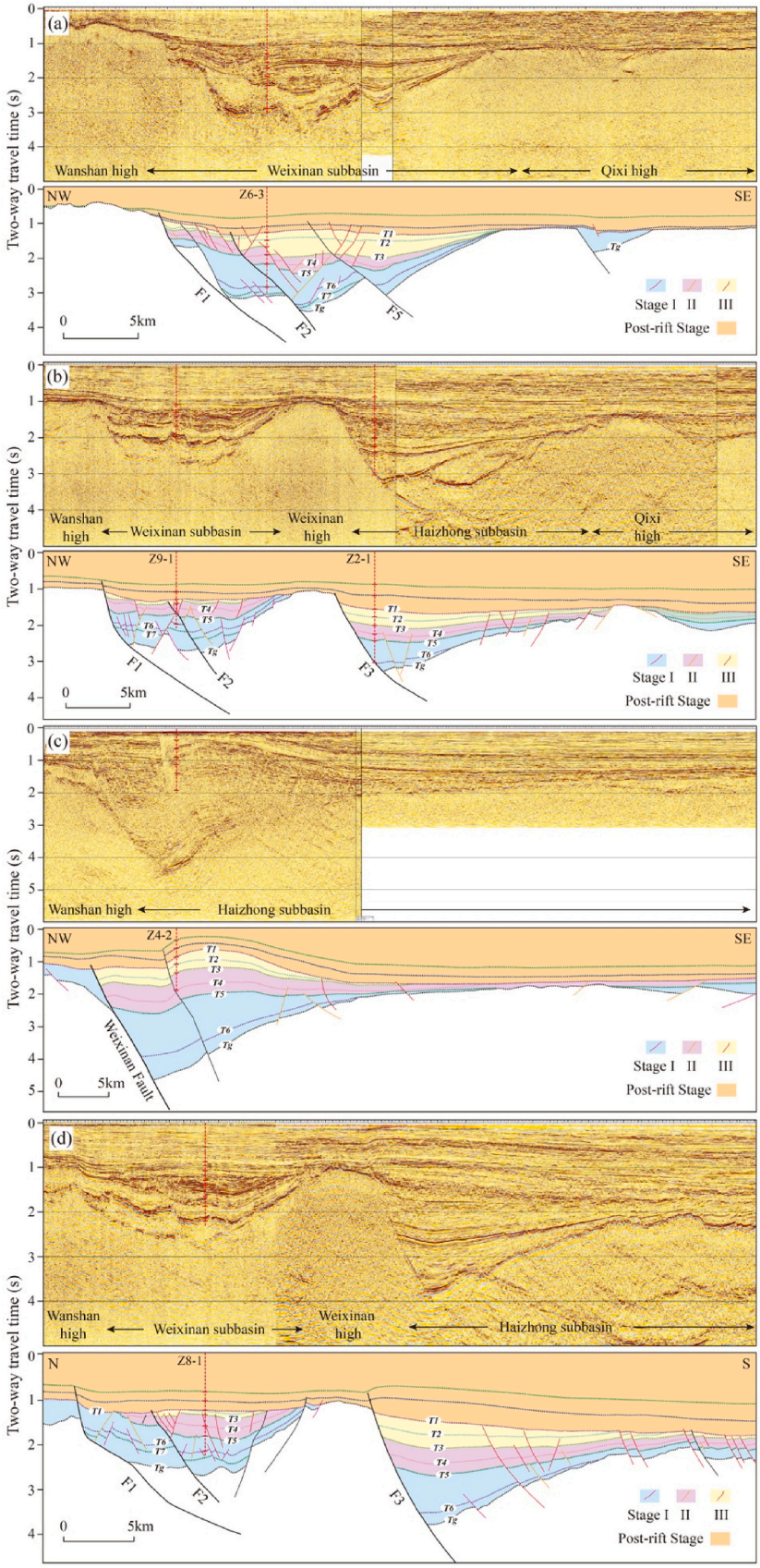

Fig. 3. Different cross-section profiles across the North subbasins of BGB (uninterpreted above and interpreted down), see locations in Fig. 1.

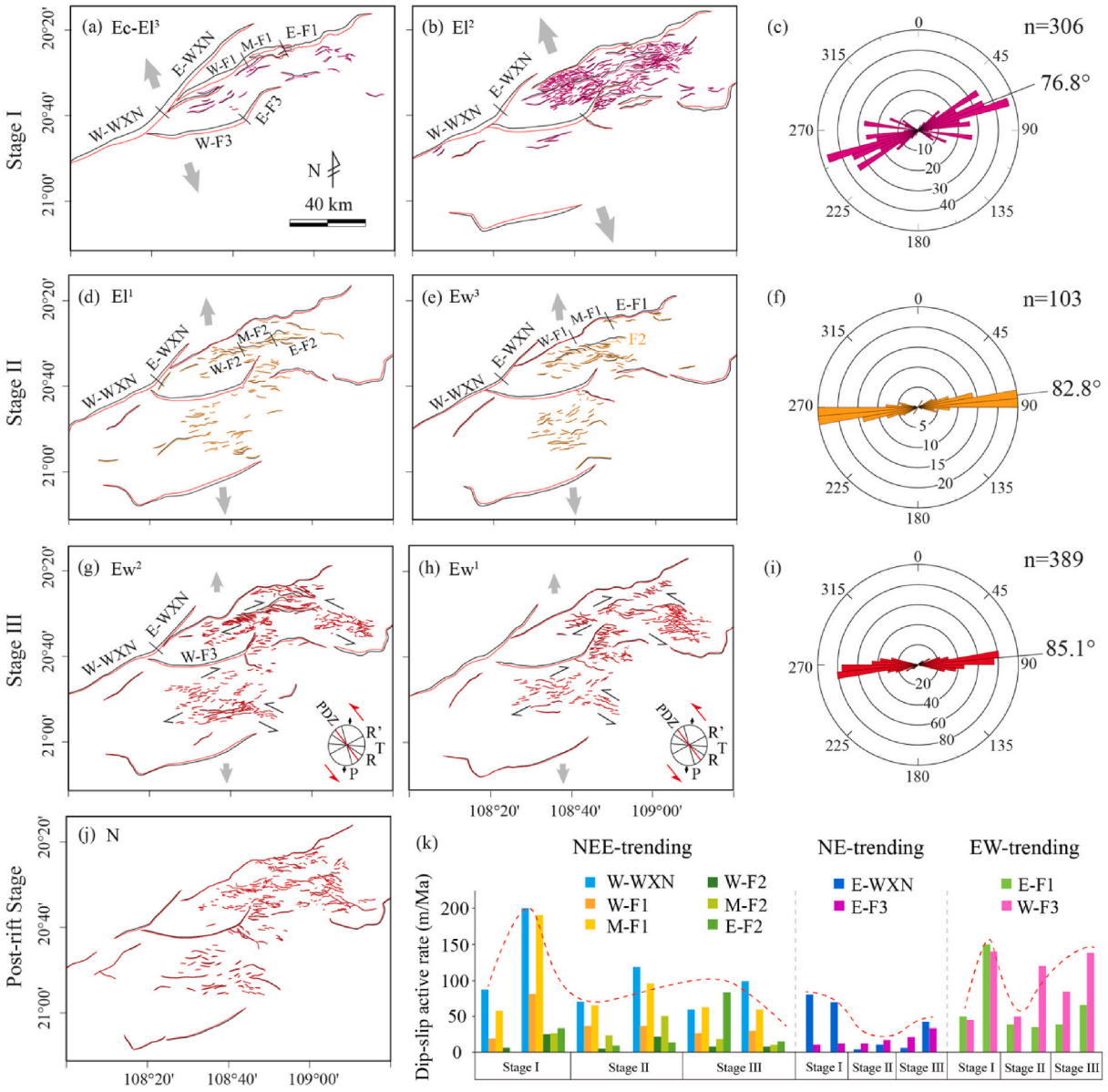

Fig. 4. Syn-depositional faults in different sedimentary stages. Average rates of active dip-slip faulting of main faults, methodology used for calculation the dip-slip faulting rate is from Huang et al. (2014). Abbreviations: W WXN: west segment of Weixinan fault, M F1: middle segment of F1, E F2: east segment of F2, etc. The red/pink/orange solid lines show the hanging wall of the fault, the black solid lines show the footwall of the fault. Fault strike azimuth-frequency distribution of the extensional faults are illustrated separately in the plots on the right. Letter n indicates the total number of minor faults in separate stages and the azimuth indicates the average strike of faults. (For interpretation of the references to colour in this figure legend, the reader is referred to the web version of this article.)

nearly N-S stretching. In this context, oblique extension acting on ENE-striking F2 fault transformed it to a shear zone consisting of a series of small-scale tensile faults (Figs. 4c, d). This change resulted in the occurrence of en echelon array horizontally (Figs. 4c, d). In the interior of the basin, the predominant NE-trending minor faults in stage I became inactive due to a change of the stress field. Instead, the principal azimuth of the minor faults changed to 82.8° and the number of faults decreased dramatically from 306 in the previous stage to 103 during stage II. Unlike the centralized NE-striking minor faults, the newborn EW-striking tensile faults are more widely spaced horizontally (Fig. 4c).

4.3.3. The NW- and ENE-conjugated strike-slip fault system

Two conjugate strike-slip fault systems can be identified during stage III and they have different orientations, being NW and ENE (Fig. 4e). The two groups of minor faults were widely distributed with a significantly increased number of 389 in the study area and they constitute the conjugate Riedel shear zone. Besides, the dip separation of main faults became smaller and the dip-slip faulting rates maintained at 50 m/Ma, indicating the weakened rifting and the transition from rifting to depression. In addition, it is worth noticing that the strike-slip deformation extends to the post-rift stage (Fig. 4g), especially during the deposition of the Nx Formation (23–18.5 Ma). Generally, the Neogene basin suffered stable subsidence and few active faults can be identified. The presence of the conjugate fault zones that consist of numerous minor faults implies that the strike-slip deformation lasted until the early Neogene, as is consistent with the trend in Yinggehai basin to the west and the Qiongdongnan basin to the south (see locations in Fig. 1a; Zhang et al., 2013; Fan, 2018).

4.3.4. Analogue modelling experimental results

Analogue modelling is an efficient way to simulate the evolution of faults at a scale and time frame that allow the visualization of how

structures develop (e.g. McClay et al., 2004; Marshak et al., 2019). Following the principle of similarity, we ran two different models to investigate how extension affected basin structures. The first model simulated NW-SE trending extension, and the second simulated NS-trending extension. The setups of the two models are shown in Fig. 5, in which the cystosepiment was used to represent the difference of basement structure of prototype basins. Each experiment was repeated 6 times, to confirm the results.

The observed BGB basin structures appear to be corroborated by the sandbox experiments. Along with the increasing amount of stretching in the SE orientation, the main faults of stage I were reproduced successfully (Fig. 5a), which is compatible with *syn*-depositional faults distribution (Figs. 4a, b). On the basis of the first simulation, the second episode was carried out with a revised boundary condition (Fig. 5b). A sustained N-S stretching was imposed on the structures of stage I, and progressively generated the major fault system of the basin. The analogue modelling result seems remarkably consistent with the syn-depositional fault distribution of stage II (Figs. 4c, d), which testified to the shift of the stress field from NW-SE to nearly N-S orientation during the syn-rift stage.

4.4. Tectonic subsidence and depocenter transition

As a crucial record of tectonic events, sedimentary fillings could well preserve the geodynamic information of the evolving sedimentary basin. The tectonic subsidence curves of different part of the basin show a spatially variable subsidence pattern (Fig. 6). The observed tectonic subsidence rates of the basin during the deposition of Ec and El^3 sub-sequences (65.5–48.6 Ma) range from 0.067 to 0.102 km m.y.$^{-1}$ (Fig. 6), coinciding with the initial rifting of the Pearl River Mouth basin to the east (Zhao et al., 2020). The observed subsidence rate reached a maximum of 0.154 km m.y.$^{-1}$ (Fig. 6) during the depositional period of El^2 sub-sequence (48.6–40.4 Ma), consistent with our observation, where both intense activity of extensional faults and synchronous occurrence of considerable minor faults marked the pinnacle of rifting. Subsequently, a new rifting stage initiated since the depositional period of El^1 Formation (40.4–30 Ma), when the mean rate of tectonic subsidence first decreased dramatically to 0.025 km m.y.$^{-1}$, and then progressively increased to 0.040 km m.y.$^{-1}$ during the deposition of Ew^{1+2} sub-sequences (30–23 Ma), indicating two distinct driving mechanisms. At the end of Paleogene, a convex-up subsidence signature is detected in most areas within the entire basin (Fig. 6), indicating a regional uplift and erosion event at about 23 Ma. The succeeding Neogene (post-rift stage) suffered stabilized sedimentation with a slow subsidence rate of 0.013 km m.y.$^{-1}$ (Fig. 6), which generated the relatively uniform strata without showing localized subsidence centers as shown in seismic sections.

The original strata thicknesses within certain periods were reconstructed after the restoration of the denudated strata, which emphasizes a feature of depocenter transition during *syn*-rift stages. During the depositional period of Ec and El^3 Formation (65.5–48.6 Ma), the depocenter with a maximum thickness of 1700 m was largely dominated by the N*E*-striking tensile faults (Fig. 7a). The initial rifting is confined in isolated subbasins that were mainly distributed along the NE-striking Weixinan fault and the west segment of F1 fault. During the depositional period of El^2 Formation (48.6–40.4 Ma), the spatial distribution of depocenter was still under the control of NE-striking faults. Whereas these earlier localized sub-subbasins began to connect to each other and two distinctive depocenters were progressively formed. The conspicuous one with a thickness about 3500 m was located along the west segment of Weixinan fault (Fig. 7b). During this period, the Weixinan high within the central basin sank below the lake level and experienced sedimentation. The average thickness of 1600 m is much larger than other observed sub-sequences reflecting the high subsidence process. Subsequently, the distribution of depocenters changed gradually since stage II (40.4–30 Ma), the range of deposits increased while the localized depocenters became inconspicuous (Fig. 7c). The barely recognizable depocenters migrated eastward gradually towards the center of the basin, roughly presenting an orientation of ENE (Fig. 7d). During stage III, new depocenters progressively formed along the E-W strike, one of which was controlled by the E-W-striking branches of F2 faults (Fig. 7e) and the other was distributed along the E-W-striking F3 fault (Fig. 7f).

5. Discussion

5.1. Episodic rifting of the BGB

The results reveal the dominant role of stress transition from NW-SE to N-S-striking extension in generating the present complex fault system, which is generally considered crucial in controlling the Paleogene *syn*-rift evolution of the North subbasins (e.g., Li et al., 2012; Tong, 2012; Ma et al., 2014). The spatial and temporal variation of the fault system determines the diversity of basin structure (Fig. 8). Based on the synthetic analyses of the stratigraphic records, *syn*-depositional fault system, and the tectonic subsidence history, the syn-rift basin formed as a result of three distinct phases of extension can be recognized. During stage I (65.5–40.4 Ma), onset of rifting is thought to have occurred at the beginning of the Cenozoic under the NW-SE-directed stretching. As the northwest boundary of the basin, the NE-trending Weixinan border fault suffered sustained extension and controlled the initial sedimentation

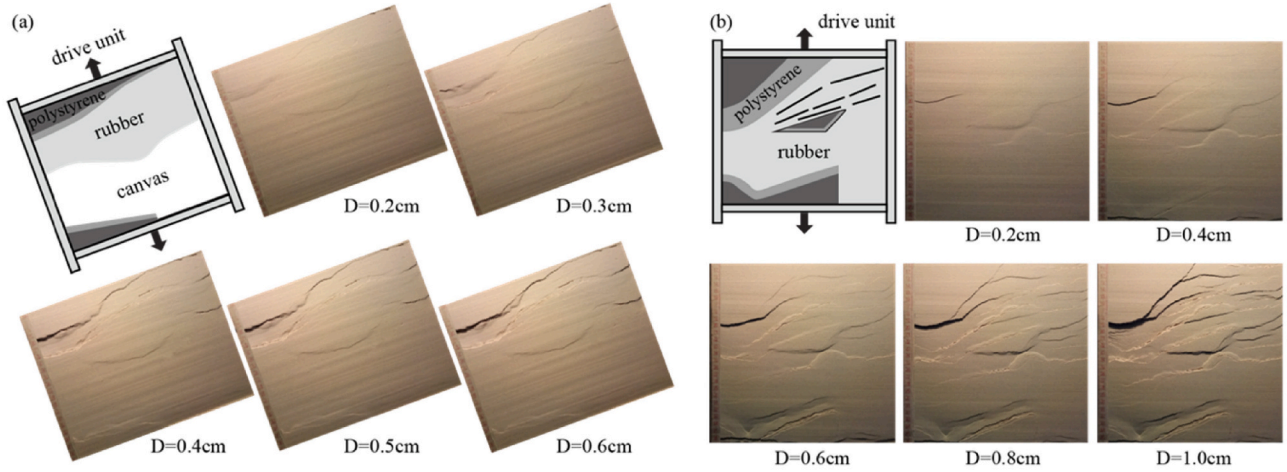

Fig. 5. Analogue modelling results. (a) Stage I simulation with NW-trending stretching. (2) Stage II simulation with NS-tending stretching on the basis of the first simulation result.

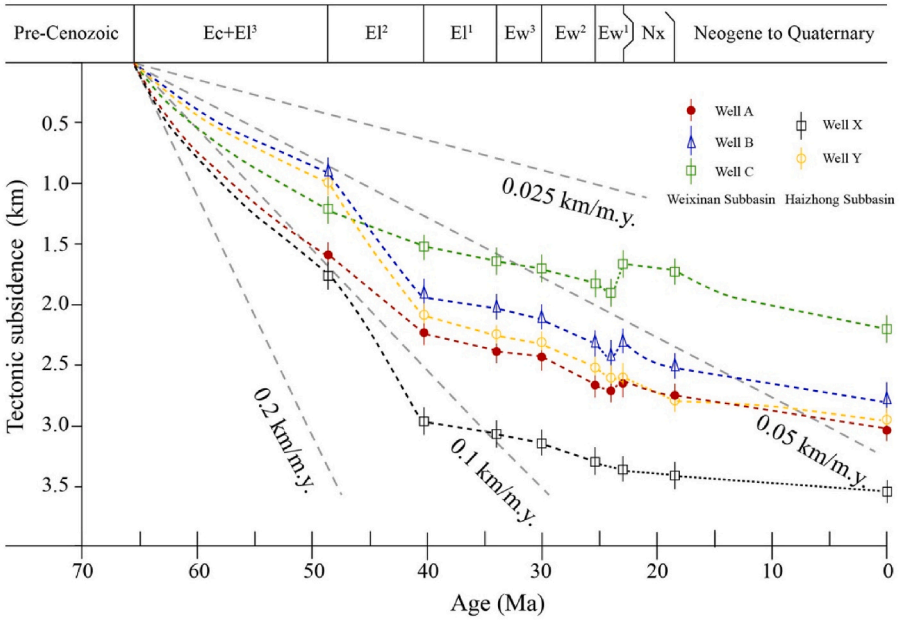

Fig. 6. Tectonic subsidence history revealed by 5 different wells. Well locations are shown in Fig. 1.

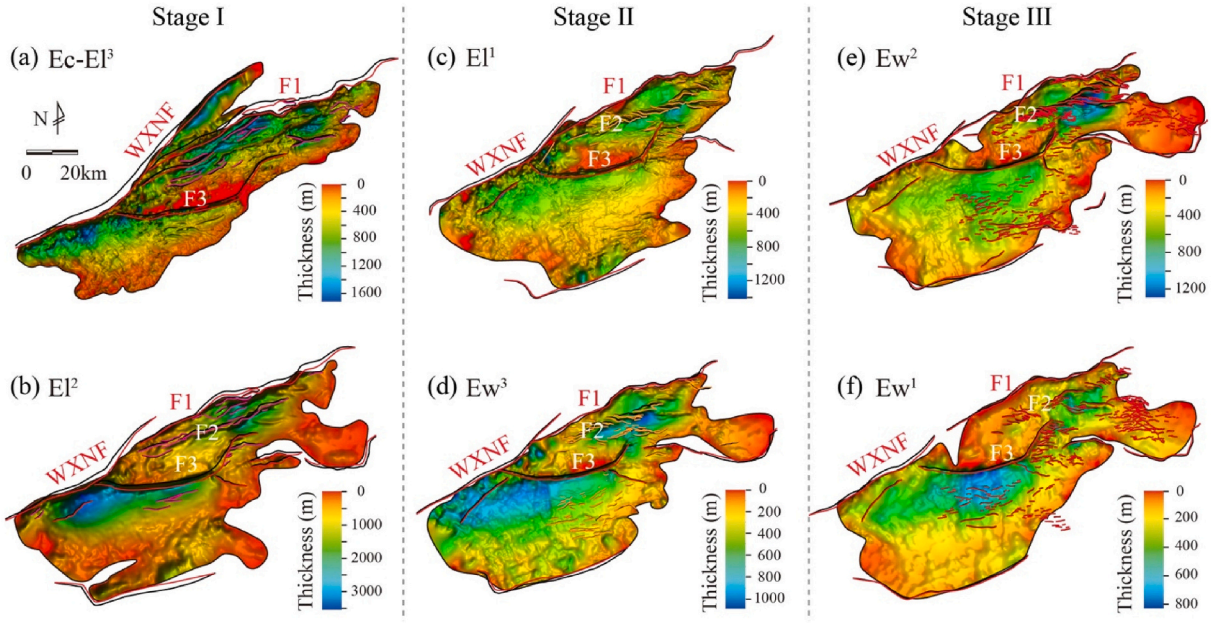

Fig. 7. Original thickness isopach maps of different Paleogene sequences. The outlines show the range of sediments in different stages. The warm colour indicates the erosion area while the cold colour shows the depocenter of the basin.

(Fig. 8a). Accompanied by the enhancement of rifting, large offset of the F1 fault controlled the evolution of the Weixinan subbasin, causing the deposition distributed along NE orientation. Additionally, the rapid subsidence (0.154 km m.y.$^{-1}$) of lacustrine sediments and occurrence of numerous NE-striking minor faults, demonstrate an episode of rapid syn-rift extension of the North subbasins of BGB.

During stage II (40.4–30 Ma), the structural pattern of the basin suffered a dramatic transition due to the change of the regional stress field. Under the newly changed NWN-SES (nearly N-S) extension, the ENE-striking fault system tends to deform logically. In particular, the typical F2 fault transformed into a shear zone consisting of several E-W striking branches due to oblique extension (Fig. 8b). The minor faults tend to distribute in E-W orientation, but the number of them decreased sharply. Meanwhile, the depocenters migrated eastward towards the central basin with a markedly decreased subsidence rate of 0.025 km m.y.$^{-1}$, suggesting an episode of weakened rifting.

Inherited from the extensional structures, the basin was reworked deeply by the transtensional deformation since stage III (30–23 Ma). Numerous minor faults developed during this period form either a flower structure or slip fault terrace structure that are attached on the main fault at depth. Judging from the map view, these faults tend to distribute in en echelon arrangements (Fig. 8c), constituting the conjugated NE-striking dextral fault zone and sinistral fault zone along NW orientation. It reflects that the conjugated strike-slip reactivation reconfigures the basin physiography during this period (Rotevatn and Peacock, 2018). Given that the shearing deformation history of fault

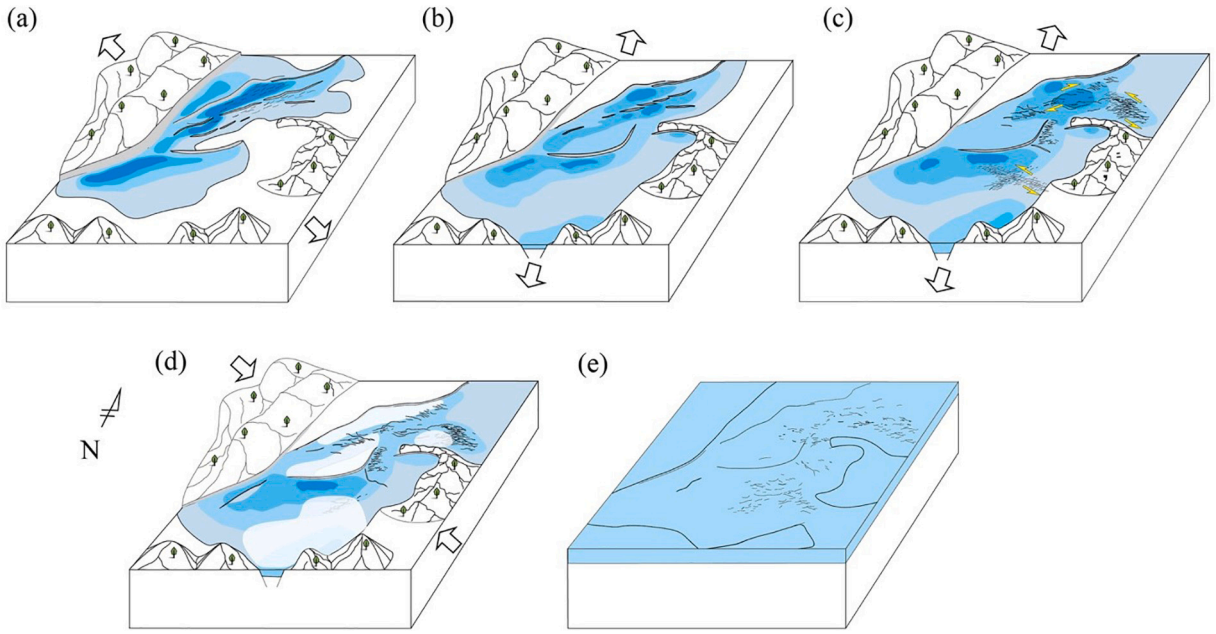

Fig. 8. Conceptual basin-evolution model of the syn-rift and post-rift phase of the North subbasins. (a) Syn-rift stage I (65.5–40.4 Ma): Initiation of the basin in a mainly NW-oriented extensional setting. (b) Syn-rift stage II (40.4–30 Ma): Stress field changed to N-S orientation, causing the basin was in oblique extension setting and the sedimentary center migrated eastward. (c) Syn-rift stage III (30–23 Ma): Strong strike-slip deformation superimposed on the N-S extension setting. (d) A shortening event at ~23 Ma: The basin suffered NW-directed compression and the broad development of angular unconformity, the white contour in Fig. 8d shows the planar distribution of angular unconformity of reversed fault. (e) Post-rift stage (since 23 Ma): The ongoing thermal subsidence with sea level rise controlled the deposition of transitional facies. During the Late Neogene, Haizhong subbasin suffered regional compression and formed broad folds. The blue contours indicate the sediment distribution in different episodes, and the grey fill shows the fault throw. (For interpretation of the references to colour in this figure legend, the reader is referred to the web version of this article.)

system is coeval with the pinnacle of the rapid displacement of the lithospheric-scale Red River Fault Zone (Rangin et al., 1995; Searle, 2006; Liu et al., 2015), there is a good reason to link the tectonic reactivation with the regional stress reorientation at that time.

At the end of Paleogene (~23 Ma), the basin suffered an intensive compression event occurred with rapid uplift and strong denudation (Fig. 8d). As a consequence, it is characterized by broad angular unconformity and antiformal negative flower structure (Huang and Liu, 2017), indicating a combined effect of extensional, compressional, and strike-slip strains. This tectonic event terminates the *syn*-rifting evolution of the basin and marks tectonic transition to post-rift stage, implying broad geodynamic significance (Franke et al., 2014).

5.2. Reactivation of NW-trending blind faults

Inherited structures in continental lithosphere, such as suture zones and young orogenic belts, tend to form crustal weaknesses that play a crucial role in determining the location and duration of deformation (Muirhead and Kattenhorn, 2018; Zhao et al., 2020). However, due to the limited resolution of the imaged basement, it is impossible to distinguish detailed pre-existing structures from the present seismic data. Alternatively, previous studies have revealed that the Mesozoic evolution of the South China was strongly influenced by the subduction of the Paleo-Pacific Plate and the multiple collisions with the micro-continental blocks of Tethys (Li et al., 2019; Duan et al., 2020), causing extensive development of NE- and NW-trending structures during the Mesozoic. In particular, several NW-trending suture zones formed coeval with the collision between the Indochina Block and South China Block during the Triassic (Shu et al., 2008), and typical NE-trending faults predominate the inland tectonics since the Jurassic (Li et al., 2019). While in the offshore basins, numerous NW-trending thrust faults, besides the ENE-striking structures, developed within a granitoid-dominated basement were detected (Ye et al., 2018). Hence, we tentatively suggest that these inherited crustal weaknesses are likely to be reactivated during the Cenozoic rifting pulses, forming the basin's current enigmatic structure.

The pre-existing structure plays a crucial role in localizing strain and influencing architecture of evolving basins (Tong, 2012; Liu et al., 2019). As described in the results, the Cenozoic structural configuration of the basin is featured by the N*E*- and ENE-striking faults, some of which are easily reactivated under the N-S oblique extension in comparison with the NW-trending Mesozoic structures, causing the earlier appearance of ENE-trending strike-slip fault zone within the basin, i.e. the typical F2 strike-slip fault during stage II.

It has been proposed that the blind fault zone is a tectonic trend zone in sedimentary layers that inherits from pre-existing faults when suffering deformation (Bellahsen and Danial, 2015; Wang et al., 2015). These pre-existing structures tend to present strike-slip deformation, accompanying a large number of secondary faults distributing in a parallel or en echelon arrangement (Fig. 9c). According to this model, we can identify some NW-oriented structural traces within the basin (Fig. 9a). Along with the regional sinistral shear deformation of the RRFZ, the NW-trending blind structures were reactivated subsequently (Fig. 9b), creating two distinctive en echelon arrays of minor faults and flower-like structures at depth. However, this kind of structure differs from the typical flower structure (Huang and Liu, 2017) due to the lack of main fault in central part (Fig. 9d). Besides, it is noteworthy that one of the blind faults developed coincidentally across the merge point of the two segments of F1 fault and the tip of F2 fault (Fig. 9a), and the other one could extend to the junction between the Weixinan fault and F3 fault (Fig. 9a). Therefore, the reactivation of the NW-trending blind faults could contribute to the various structural configuration of the basin. Such a scenario appears to be corroborated by the same geological phenomenon in the neighboring Wushi subbasin (located in South subbasins of the BGB, Hu et al., 2016), where a conspicuous blind fault zone developed, linking to the NW-trending fault zone in this study. Here, we interpret these large-scale NW-trending blind fault zones to constitute the R-shears while the ENE-trending fault zones form

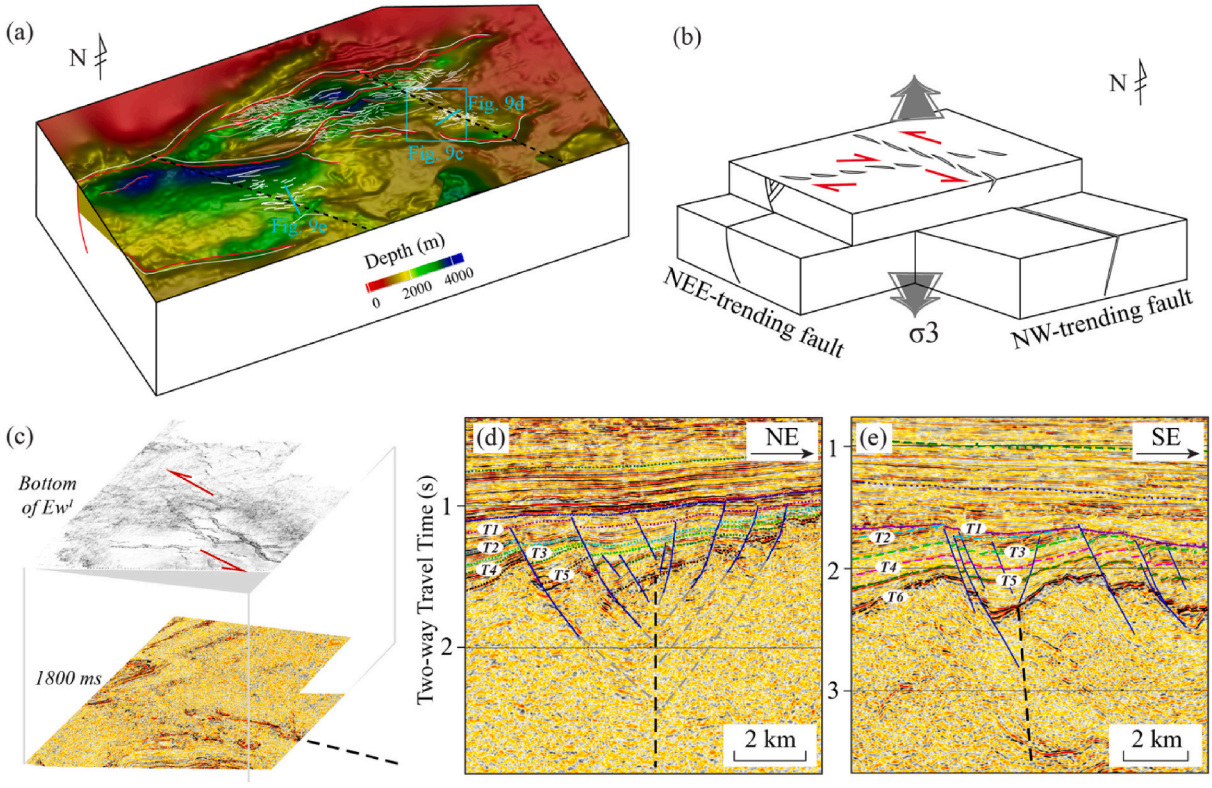

Fig. 9. (a) Structural configuration of syn-rift basin. The red and white curves indicate the syn-depositional faults during rifting. The black dash lines show the NW-trending blind faults. (b) Conceptual model of blind NW-trending fault when suffered strike-slip reactivation. (c) Horizonal slice of 3D seismic data. Location is shown in Fig. 9a. (d) (e) Cross-sections that show the development of small-scale faults, see locations in Fig. 9a, the black dash line indicates the NW-trending blind faults. (For interpretation of the references to colour in this figure legend, the reader is referred to the web version of this article.)

antithetic R'-shears of a sinistral Riedel shear zone (Schreurs, 1994; Davis et al., 2000; Coelho et al., 2006). We suggest that these strike-slip deformation structures within the basin were reactivated from inherited structures, implying a synergistic effect of oblique extension and sinistral shear deformations.

5.3. Implication for regional tectonics

The architecture of the evolving basin reflects the transition of regional stress field and the overprint of strike-slip deformation. Along with the rapid extrusion of the Indochina block (Zhang et al., 2013; Müller et al., 2016), the large-scale sinistral displacement of the Red River Fault Zone took place with an intensive period from the late Eocene (Zhu et al., 2009; Zhao et al., 2018), resulting in extensive transtensional deformation within the basin. In addition, the ongoing subduction of the Proto-SCS underneath the Borneo could generate a continuous N-S directed slab pull force to the basin. Meanwhile, the seafloor spreading of East Sub-basin initiated and it led to the termination of rifting in Pearl River Mouth basin (Savva et al., 2014; Sibuet et al., 2016), but it barely affected the evolution of the BGB due to the lack of orthogonal ridge push. Influenced by the synergistic effects of these tectonic events, the pre-existing faults experienced strike-slip reactivation and the basin is characterized by continuously ENE-striking rifting and extensive strike-slip deformation.

Accompanied with the continued indentation of the rigid Indian Plate into Eurasia (Tapponnier et al., 1990), the subducted slab changed the motion to N30° at ~23 Ma with a decreased velocity (Lee and Lawver, 1995). The nearly orthogonal convergence may induce the adjustment of WNW-directed RRFZ's activity, and a few tens of kilometers of right-lateral motion of the RRFZ may occur during the late stage of opening of the SCS (Sibuet et al., 2016). Meanwhile, the seafloor spreading of the SCS jumped from the East Sub-basin to Southwest Sub-basin with a reorientation of the spreading ridge from E-W to NE-SW (Taylor and Hayes, 1983; Briais et al., 1993; Li et al., 2015). From the east side, the Philippines Sea Plate and the Pacific Plate subducted beneath the Eurasia Plate with a WNW-directed acceleration (Müller et al., 2016; Jicha and Kay, 2018). These above tectonic reconfigurations may provide a NW-SE compression to the region. Considering that the end-rift unconformity of different basins diachronously occurred along both margins of the SCS (Franke et al., 2014; Savva et al., 2014), coinciding with westward migration of the seafloor spreading (Sun et al., 2009). We suggest that the adjustment of RRFZ displacement and the ridge push resulted from the seafloor spreading contributed to the end-rift tectonism. After that, the basin passed into the post-rift stage, during which it suffered stable and extensive thermal subsidence with very weak or no faulting activity.

6. Conclusions

Updated high-resolution seismic data and borehole data allow a detailed tectono-sedimentary analysis of the North subbasins in Beibu Gulf basin. Based on the identification of several key unconformities related to different tectonic events, three distinct phases of rifting of the basin could be recognized. The evolving structures reflect the overprint of extensional and shearing deformation.

We find that BGB is a rift basin associated with multi-phase extension. It is characterized by NE/ENE-trending rift system due to northwest-southeast stretching during the early stage of basin evolution. And then the structural configuration of the basin changed to ENE/EW-striking as a result of the newly changed stress of north-south stretching.

Influenced by the reorientation of regional stress filed acting on pre-existing faults, the basin was reworked deeply by the ENE- and NW-trending conjugate strike-slip deformation. We suggest that reactivation of NW-trending blind faults was triggered by the regional shear

activity and oblique extension acting on the Mesozoic pre-existing structures.

Declaration of Competing Interest

The authors declare that they have no known competing financial interests or personal relationships that could have appeared to influence the work reported in this paper.

Acknowledgements

This research is financially supported by the National Natural Science Foundation of China (42072169), China National Science and Technology Major Project (2016ZX05024-002-001) and the China Scholarship Council (201706450007). We thank the Editor-in-Chief, Prof. Zheng-Xiang Li, and three anonymous reviewers for their significant comments and suggestions, which substantially improved the manuscript. We sincerely thank Prof. Stephen Marshak at UIUC for the discussions and substantial improvement for the original manuscript. We thank the Zhanjiang Branch of CNOOC for providing seismic data and well data for this work.

References

Allen, P.A., Allen, J.R., 2013. Basin Analysis: Principles and Applications to Petroleum Play Assessment. Wiley-Blackwell, Oxford.

Bellahsen, N., Danial, J.M., 2015. Fault reactivation control on normal fault growth: an experimental study. J. Struct. Geol. 27 (4), 769–780. https://doi.org/10.1016/j.jsg.2004.12.003.

Briais, A., Patriat, P., Tapponnier, P., 1993. Updated interpretation of magneticanomalies on seafloor spreading stages in the South China Sea: implications for the Tertiary tectonics of Southeast Asia. J. Geophys. Res. 98 (B4), 6299–6328.

Cao, S., Neubauer, F., Liu, J., Genser, J., Leiss, B., 2011. Exhumation of the diancang Shan metamorphic complex along the ailao Shan-Red river belt, southwestern Yunnan, China: evidence from 40Ar/39Ar thermochronology. J. Asian Earth Sci. 42, 525–550.

Chen, M., Shi, X., Ren, Z., Xu, Z., Liu, K., Liu, H., 2019. Late Cenozoic subsidence and sedimentary features of the basins in the northwestern South China Sea: implications for the development of the deep anomalous progress. Chin. J. Geophys. 62 (2), 587–603 (in Chinese with English abstract).

Clift, P.D., Sun, Z., 2006. The sedimentary and tectonic evolution of the Yinggehai-Song Hong Basin and the Southern Hainan margin, South China Sea: implications for Tibetan uplift and monsoon intensification. J. Geohys. Res. 111, 1–28. https://doi.org/10.1029/2005JB004048.

Coelho, S., Passchier, C., Marques, F., 2006. Riedel-shear control on the development of pennant veins: Field example and analogue modeling. J. Struc. Geol. 28, 1658–1669.

Cullen, A., Reemst, P., Henstra, G., Gozzard, S., Anandaroop, R., 2010. Rifting of the South China Sea: new perspective. Pet. Geosci. 16, 273–282.

Davis, G.H., Bump, A.P., Garcia, P.E., Ahlgren, S.G., 2000. Conjugate Riedel deformation band shear zones. J. Struct. Geol. 22 (2), 169–190.

Ding, W., Sun, Z., Dadd, K., Fang, Y., Li, J., 2018. Structures within the oceanic crust of the central South China Sea basin and their implications for oceanic accretionary processes. Earth Planet. Sci. Lett. 488, 115–125. https://doi.org/10.1016/j.epsl.2018.02.011.

Ding, W., Sun, Z., Mohn, G., Nirrengarten, M., Tugend, J., Manatschal, G., Li, J., 2020. Lateral evolution of the rift-to-drift transition in the South China Sea: evidence from multi-channel seismic data and IODP Expeditions 367&368 drilling results. Earth Planet. Sci. Lett. 531, 115932. https://doi.org/10.1016/j.epsl.2019.115932.

Duan, L., Meng, Q., Wu, G., Yang, Z., Wang, J., Zhan, R., 2020. Nanpanjiang basin: a window on the tectonic development of South China during Triassic assembly of the southeastern and eastern Asia. Gondwana Res. 78, 189–209.

Fan, C., 2018. Tectonic deformation features and petroleum geological significance in Yinggehai large strike-slip basin, South China Sea. Pet. Explor. Dev. 45 (2), 204–214.

Franke, D., Savva, D., Pubellier, M., Steuer, S., Mouly, B., Auxietre, J., Meresse, F., Chamot-Rooke, N., 2014. The final rifting evolution in the South China Sea. Mar. Petrol. Geol. 58, 704–720. https://doi.org/10.1016/j.marpetgeo.2013.11.020.

Gao, Z., Yang, X., Hu, C., Wei, L., Jiang, Z., Yang, S., Fan, Y., Xue, Z., Yu, H., 2019. Characterizing the pore structure of low permeability Eocene Liushagang Formation reservoir rocks from Beibuwan Basin in northern South China Sea. Mar. Petrol. Geol. 99, 107–121.

Gilley, L.D., Harrison, T.M., Leloup, P.H., Ryerson, F.J., Lovera, O.M., Wang, J., 2003. Direct dating of left-lateral deformation along the red river shear zone, China and Vietnam. J. Geophys. Res. 108 (ECV14.1-ECV14.21).

Hall, R., Spakman, W., 2015. Mantle structure and tectonic history of SE Asia. Tectonophysics 658, 14–45. https://doi.org/10.1016/j.tecto.2015.07.003.

Hampel, A., Adam, J., Kukowski, N., 2004. Response of tectonically erosive south Peruvian forearc to subduction of the Nazca Ridge: Analysis of three dimensional analogue experiments. Tectonics 23, TC5003.

Hu, B., Wang, L., Yan, W., Liu, S., Cai, D., Zhang, G., Zhong, K., Pei, J., Sun, B., 2013. The tectonic evolution of the Qiongdongnan Basin in the northern margin of the South China Sea. J. Asian Earth Sci. 77, 163–182.

Hu, D., Deng, Y., Zhang, J., Zuo, Q., He, W., 2016. Palaeogene fault system and hydrocarbon accumulation in east Wushi sag. J. Southwest Petrol. Univ. 38 (4), 27–36 (in Chinese with English abstract).

Huang, L., Liu, C., 2017. Three Types of Flower Structures in a Divergent-Wrench Fault Zone. J. Geophys. Res. 122, 10,478–10,497.

Huang, B., Tian, H., Wilkins, R.W.T., Xiao, X., Li, L., 2013. Geochemical characteristics, palaeoenvironment and formation model of Eocene organic-rich shales in the Beibuwan Basin, South China Sea. Mar. Petrol. Geol. 48, 77–89. https://doi.org/10.1016/j.marpetgeo.2013.07.012.

Huang, L., Liu, C., Wang, Y., Zhao, J., Mountney, N.P., 2014. Neogene–Quaternary postrift tectonic reactivation of the Bohai Bay Basin, eastern China. AAPG Bull. 98, 1377–1400. https://doi.org/10.1306/03071413046.

Jicha, B., Kay, S.M., 2018. Quantifying arc migration and the role of forearc subduction erosion in the central Aleutians. J. Volc. Geothermal Res 360, 84–99. https://doi.org/10.1016/j.jvolgeores.2018.06.016.

Lee, T.Y., Lawver, L.A., 1995. Cenozoic plate reconstruction of Southeast Asia. Tectonophysics 251, 85–138.

Lei, C., Ren, J., Sternai, P., Fox, M., Willett, S., Xie, X., Clift, P.D., Liao, J., Wang, Z., 2015. Structure and sediment budget of Yinggehai–Song Hong basin, South China Sea: implications for Cenozoic tectonics and river basin reorganization in Southeast Asia. Tectonophysics 655, 177–190.

Leloup, P.H., Arnaud, N., Lacassin, R., Kienast, J.R., Harrison, T.M., Trong, T.T.P., Replumaz, A., Tapponnier, P., 2001. New constraints on the structure, thermochronology, and timing of the Ailao Shan-Red River Shear Zone, SE Asia. J. Geophys. Res. Solid Earth 106, 6683–6732.

Li, Z.X., Li, X.H., 2007. Formation of the 1300-km-wide intracontinental orogen and postorogenic magmatic province in Mesozoic South China: a flat-slab subduction model. Geology 35, 179–182.

Li, C., Zhang, G., Liang, J., Zhao, Z., Xu, J., 2012. Characteristics of fault structure and its control on hydrocarbons in the Beibuwan Basin. Acta Pet. Sin. 33 (2), 195–203 (in Chinese with English abstract).

Li, C., Li, J., Ding, W., Franke, D., Yao, Y., Shi, H., Pang, X., Cao, Y., Lin, J., Kulhanek, D. K., 2015. Seismic stratigraphy of the central South China Sea basin and implications for neotectonics. J. Geophys. Res. 120 (3), 1377–1399. https://doi.org/10.1002/2014JB011686.

Li, S., Suo, Y., Li, X., Zhou, J., Santosh, M., Wang, P., Wang, G., Guo, L., Yu, S., Lan, H., Dai, L., Zhou, Z., Cao, X., Zhu, J., Liu, B., Jiang, S., Wang, G., Zhang, G., 2019. Mesozoic tectono-magmatic response in the East Asian ocean-continent connection zone to subduction of the Paleo-Pacific Plate. Earth Sci. Rev. 192, 91–137. https://doi.org/10.1016/j.earscirev.2019.03.003.

Liu, J., Chen, X., Wu, W., Tang, Y., Tran, M., Nguyen, Q., Zhang, Z., Zhao, Z., 2015. New tectono-geochronological constraints on timing of shearing along the Ailao Shan-Red River shear zone: implications for genesis of Ailao Shan gold mineralization. J. Asian Earth Sci. 103, 70–86.

Liu, Y., Wu, Z., Liu, L., Zhang, X., Li, W., Chen, S., Hao, X., 2019. Cenozoic fault system and tectonic framework in Chengbei Sag and its adjacent areas, Bohai Bay basin. Geotectonic. et Metall. 43 (6), 1133–1143 (in Chinese with English abstract).

Liu, L., Peng, D., Liu, L., Chen, L., Li, S., Wang, Y., Cao, Z., Feng, M., 2021a. East Asian lithospheric evolution dictated by multistage Mesozoic flat-slab subduction. Earth Sci. Rev. 217, 103621.

Liu, Y., Wu, Z., Yan, S., Yang, X., Ping, M., Zhang, M., 2021b. New insight into the origin of horsetail-like structure in Beibu depression, Beibu Gulf Basin. J. China Univ. Min. Tech. 50 (1), 39–51 (in Chinese with English abstract).

Ma, Y., Li, S., Zhang, B., Gong, S., Liu, X., Yu, S., Wang, X., Zhao, S., 2014. Unconformities in the Beibuwan Basin and their implications for tectonic evolution. Mar. Geol. Quat. Geol. 33 (2), 63–72 (in Chinese with English abstract).

Marshak, S., Haq, S.S.B., Sen, P., 2019. Ramp initiation in fold-thrust belts: Insight from PIV analysis of sandbox models. J. Structural Geol. 118, 308–323. https://doi.org/10.1016/j.jsg.2018.11.006.

McClay, K.R., White, M.J., 1995. Analogue modelling of orthogonal and oblique rifting. Mar. Petrol. Geol. 12 (2), 137–151. https://doi.org/10.1016/0264-8172(95)92835-K.

McClay, K.R., Whitehouse, P., Dooley, T., Richards, M., 2004. 3D evolution of fold and thrust belts formed by oblique convergence. Mar. Petrol. Geol. 21, 857–877.

Morley, C.K., 2002. A tectonic model for the Tertiary evolution of strike-slip faults and rift basins in SE Asia. Tectonophysics 347 (4), 189–215.

Muirhead, J.D., Kattenhorn, S.A., 2018. Activation of preexisting transverse structures in an evolving magmatic rift in East Africa. J. Struct. Geol. 106, 1–18. https://doi.org/10.1016/j.jsg.2017.11.004.

Müller, R.D., Seton, M., Zahirovic, S., Williams, S.E., Matthews, K.J., Wright, N.M., Shephard, G., Maloney, K., Barnett-Moore, N., Hosseinpour, M., 2016. Ocean Basin Evolution and Global-Scale Plate Reorganization events since Pangea Breakup. Annu. Rev. Earth Planet. Sci. 44 (1), 107–138. https://doi.org/10.1146/annurev-earth-060115-012211.

Panien, M., Schreurs, G., Pfiffner, A., 2006. Mechanical behaviour of granular materials used in analogue modelling: insights from grain characterisation, ring-shear tests and analogue experiments. J. Struct. Geol. 28 (9), 1710–1724. https://doi.org/10.1016/j.jsg.2006.05.004.

Rangin, C., Klein, M., Roques, D., Pichon, X.L., 1995. The Red River fault system in the tonkin Gulf, Vietnam. Tectonophysics 243, 209–222.

Ren, J., 2018. Genetic dynamics of China offshore Cenozoic basins. Earth Sci. 43 (10), 3337–3361 (In Chinese with English abstract).

Ren, J., Tamaki, K., Li, S., Zhang, J., 2002. Late Mesozoic and Cenozoic rifting and its dynamic setting in Eastern China and adjacent areas. Tectonophysics 344, 175–205. https://doi.org/10.1016/S0040-1951(01)00271-2.

Rotevatn, A., Peacock, D.P., 2018. Strike-slip reactivation of segmented normal faults: Implications for basin structure and fluid flow. Basin Res. 30, 1264–1279. https://doi.org/10.1111/bre.12303.

Savva, D., Pubellier, M., Franke, D., Chamot-Rooke, N., Meresse, F., Steuer, S., Auxietre, J.L., 2014. Different expressions of rifting on the South China Sea margins. Mar. Petrol. Geol. 58, 579–598. https://doi.org/10.1016/j.marpetgeo.2014.05.023.

Schreurs, G., 1994. Experiments on strike-slip faulting and block rotation. Geology 22, 567–570.

Searle, M.P., 2006. Role of the Red River Shear zone, Yunnan and Vietnam, in the continental extrusion of SE Asia. J. Geol. Soc. Lond. 163 (6), 1025–1036. https://doi.org/10.1144/0016-76492005-144.

Sheaf, M.A., Serpa, L., Pavlis, T.L., 2003. Exhumation rates in the St. Elias Mountains. Alaska. Tectonophysics 367 (1–2), 1–11. https://doi.org/10.1016/S0040-1951(03)00124-0.

Shu, L., Faure, M., Wang, B., Zhou, X., Song, B., 2008. Late Palaeozoic-early Mesozoic geological features of South China: response to the Indosinian collision events in Southeast Asia. Compt. Rendus Geosci. 340, 151–165.

Sibuet, J.C., Yeh, Y.C., Lee, C.S., 2016. Geodynamics of the South China Sea. Tectonophysics 692, 98–119. https://doi.org/10.1016/j.tecto.2016.02.022.

Sun, Z., Zhong, Z., Zhou, D., Cai, D., Li, X., Wu, S., Jiang, J., 2009. 3D analogue modeling of the South China Sea: a discussion on breakup pattern. J. Asian Earth Sci. 34 (4), 544–556. https://doi.org/10.1016/j.jseaes.2008.09.002.

Sun, X., Zhang, X., Zhang, G., Lu, B., Yue, J., Zhang, B., 2014. Texture and tectonic attribute of Cenozoic basin basement in the northern South China Sea. Sci. China Earth Sci. 57, 1199–1211.

Sun, Z., Ding, W., Zhao, X., Qiu, N., Lin, J., Li, C.F., 2019. The latest spreading periods of the South China Sea: New constraints from macrostructure analysis of IODP Expedition 349 cores and geophysical data. J. Geophys. Res. https://doi.org/10.1029/2019JB017584.

Tapponnier, P., Lacassin, R., Leloup, P.H., Sharer, U., Zhong, D., Wu, H., Liu, X., Ji, S., Zhang, L., Zhong, J., 1990. The Ailao Shan-Red River metamorphic belt: Tertiary left lateral shear between Sundaland and South China. Nature 343, 431–437.

Taylor, B., Hayes, D.E., 1983. Origin and history of the South China Sea Basin. In: Hayes, D.E. (Ed.), The Tectonic and Geologic Evolution of Southeast Asian Seas and Islands, Part, vol. 2, pp. 23–56.

Tian, F., Luo, X., Zhang, W., 2019. Integrated geological-geophysical characterizations of deeply buried fractured-vuggy carbonate reservoirs in Ordovician strata, Tarim Basin. Mar. Petrol. Geol. 99, 292–309.

Tong, H., 2012. Sandbox modeling of fault formation and evolution in the Weixinan Sag, Beibuwan Basin. China. Petrol. Sci. 9 (2), 121–128.

Van Hinte, J.E., 1978. Geohistory analysis-application of micropaleontology to exploration geology. AAPG Bull. 62, 201–222.

Wang, W., Zhou, W., Shan, X., Liu, Yu., 2015. Characteristics of hidden fault zone and its significance in geology in sedimentary basin. J. Central South Univ. 46 (6), 2236–2243 (in Chinese with English abstract).

Wei, C., He, Y., Geng, C., Wang, Z., 2008. Faulting mechanism in Northern depression of the Beibuwan Basin. China. Geotectonic. et Metall. 32 (1), 28–35 (in Chinese with English abstract).

Xu, S., Bai, X., Zeng, Q., Lin, M., Huang, Y., Pan, H., 2016. GeoEast integrated seismic processing and interpretation system. Computer Appl. Petrol. 24 (3), 6–11 (in Chinese with English abstract).

Ye, Q., Mei, L., Shi, H., Camanni, G., Shu, Y., Wu, J., Yu, L., Deng, P., Li, G., 2018. The late cretaceous tectonic evolution of the South China Sea area: an overview, and new perspectives from 3D seismic reflection data. Earth Sci. Rev. 187, 186–204. https://doi.org/10.1016/j.earscirev.2018.09.013.

Yin, A., 2010. Cenozoic tectonic evolution of Asia: a preliminary synthesis. Tectonophysics 488 (1–4), 293–325. https://doi.org/10.1016/j.tecto.2009.06.002.

Zampetti, V., Schlager, W., Von Konijnenburg, J.H., Everts, A.J., 2004. Architecture and growth history of a Miocene carbonate platform from 3D seismic reflection data; Luconia province, offshore Sarawak. Malaysia. Mar. Petrol. Geol. 21 (5), 517–534.

Zhang, N., Li, Z.X., 2018. Formation of mantle "lone plumes" in the global downwelling zone — a multiscale modelling of subduction-controlled plume generation beneath the South China Sea. Tectonophysics 723, 1–13.

Zhang, C., Wang, Z., Sun, Z., Sun, Z., Liu, J., Wang, Z., 2013. Structural differences between the western and eastern Qiongdongnan Basin: evidence of Indochina block extrusion and South China Sea seafloor spreading. Mar. Geophys. Res. 34, 309–323. https://doi.org/10.1007/s11001-013-9187-3.

Zhao, Z., Sun, Z., Sun, L., Wang, Z., Sun, Z., 2018. Cenozoic tectonic subsidence in the Qiongdongnan Basin, northern South China Sea. Basin Res. 30, 269–288. https://doi.org/10.1111/bre.12220.

Zhao, F., Alves, T.M., Xia, S., Li, W., Wang, L., Mi, L., Wu, S., Cao, J., Fan, C., 2020. Along-strike segmentation of the South China Sea margin imposed by inherited pre-rift basement structures. Earth Planet. Sci. Lett. 530, 115862. https://doi.org/10.1016/j.epsl.2019.115862.

Zhu, M., Graham, S., McHargue, T., 2009. The Red River fault zone in the Yinggehai Basin, South China Sea. Tectonophysics 476, 397–417.

Zuo, Y., Qiu, N., Zhang, Y., Li, C., Li, J., Guo, Y., Pang, X., 2011. Geothermal regime and hydrocarbon kitchen evolution of the offshore Bohai Bay Basin, North China. AAPG Bull. 95 (5), 749–769. https://doi.org/10.1306/09271010079.